The molecular origin of the OCP-dependent non-photochemical quenching mechanism in cyanobacteria

Nicoletta Liguori[1,], Ivo H.M. van Stokkum[1], Fernando Muzzopappa[2], John T. M. Kennis[1], Diana Kirilovsky[2], Roberta Croce[1,*]*

[1]Department of Physics and Astronomy and Institute for Lasers, Life and Biophotonics, Faculty of Sciences, Vrije Universiteit Amsterdam, Amsterdam, The Netherlands

[2]Institute for Integrative Biology of the Cell (I2BC), CNRS, CEA, Université Paris-Sud, Université Paris-Saclay, Gif sur Yvette, 91198, France

[*]To whom correspondence should be addressed:
N.L., n.liguori@vu.nl; R.C., r.croce@vu.nl

Cyanobacteria were the first microorganisms that released oxygen into the atmosphere billions of years ago. To do it safely under intense sunlight, they developed strategies that prevent photooxidation in the photosynthetic membrane. One of these strategies is accomplished by regulating the light-harvesting activity of their antenna complexes – the phycobilisomes – via the orange-carotenoid protein (OCP). This water-soluble protein encapsulates a ketocarotenoid and is photoactive. Under strong irradiance, OCP interacts with the phycobilisomes and triggers non-photochemical quenching (NPQ), a mechanism that safely dissipates overexcitation in the membrane. To date, the mechanism of action of OCP in triggering NPQ is unknown. We here applied ultrafast spectroscopy on the active domain of OCP bound to the phycobilisome core. Our results demonstrate that the binding to the phycobilisomes modifies the structure of the ketocarotenoid. We show that this molecular switch activates NPQ, by enabling energy transfer from the antenna pigments to the ketocarotenoid.

Introduction

Life under fluctuating light conditions is not without peril for photosynthetic organisms. Sudden spikes in sunlight intensity can saturate the photosynthetic electron transport chain, creating an excess of photoexcitations in the thylakoid membrane. The unprocessed photoexcitations may ultimately lead to photooxidative damage. Through evolution, however, photosynthetic organisms provided themselves with an effective set of molecular tools, which allows them to swiftly dissipate the excess excitation energy as heat. One of these photoprotective processes is known as non-photochemical quenching (NPQ) and, in distinct forms, is present in plants, algae and cyanobacteria[1,2].

Cyanobacteria, in particular, are the most abundant oxygenic photoautotrophs on Earth[3] and, likely, the most ancient organisms that required molecular strategies to prevent photooxidation[4]. Their light-harvesting machinery consists of >10[3] kDa supramolecular complexes called phycobilisomes (PBS), composed of different types of phycobiliproteins that covalently bind phycobilin pigments[5]. A typical structure of a cyanobacterial PBS is reported in **Fig. 1.A**. In the case of *Synechocystis* sp. PCC *6803*, a model organism for photosynthesis studies in

1

cyanobacteria, PBS are composed of a central core (CK), consisting of 3 cylinders of allophycocyanin (APC), from which several rods of phycocyanin radiate[6]. PBS are water soluble and the assembly of the whole structure (CK plus rods) is arranged by pigment-less linker proteins. PBS are attached via the two basal APC cylinders to the stromal side of the thylakoid membrane, in functional proximity to the photosystems[7]. Each APC cylinder consists of 4 disks of trimeric proteins, binding a total of 24 phycocyanobilins. Most phycocyanobilins emit at 660 nm (APC660), while up to 2 pigments in the basal cylinders emit at ≈680 nm (APC680). The latter ones represent the lowest energy sites of the whole PBS and are responsible for funnelling the excitation energy to the photosystems (**Fig. 1.A**).

 The NPQ mechanism in cyanobacteria is activated by strong blue-green light, which triggers the interaction between a carotenoid-binding protein, called orange-carotenoid protein (OCP), and the PBS[8,9]. OCP is a 35 kDa water-soluble protein composed of an α/β-fold C-terminal domain (CTD) and an α-helical N-terminal domain (NTD), connected via a flexible linker[10] (**Fig. 1.B**). A single ketocarotenoid (typically 3'hydroxyechinenone, canthaxanthin or echinenone)[10–13] is encapsulated via hydrogen bonds in the C-terminal domain[10]. OCP is a photoactive protein[14]: *i.e.* strong blue-green light is absorbed by the ketocarotenoid, which in turn detaches from CTD and translocates 1.2 nm into the NTD domain[14–16]. This event is followed by dissociation and separation of the NTD and CTD[17–20]. This final arrangement represents the active form of OCP, which is called OCP^R, while the inactive form is called OCP^O. The superscripts R and O indicate the red and orange colors of the two OCP forms, and different intermediate states have been proposed to be populated by the ketocarotenoid in order to establish the OCP^R state[16,21–23]. OCP^R has been proposed to bind to the basal APC in CK via the carotenoid-binding NTD (holo-NTD)[24], triggering quenching in the PBS (**Fig. 1.C**)[25,26]. This proposal was recently validated by the first cryo-EM structure of a quenched OCP-PBS complex[27]. This structure shows 4 OCP binding in the form of 2 dimers to the 2 basal APC cylinders.

 Although the key players of NPQ in cyanobacteria have been identified[8,27,28], key questions remain unanswered to date: i.e. i) what is the quenching mechanism induced by OCP? ii) Is a molecular switch of the carotenoid bound to OCP the "ignition key" of NPQ in cyanobacteria? We here address both points using ultrafast spectroscopy and compartmental model fitting, applied to an *in vitro* system prototypical of OCP-dependent NPQ in cyanobacteria.

Results and discussion
Binding of NTD to CK generates strong quenching. NTD binding canthaxanthin was synthesised in *E. coli*[12], while CK was isolated from a mutant of Synechocystis PCC 6803 lacking the rods[29,30]. A complex composed of NTD bound to CK (CK-NTD) was obtained as described in the Methods. This work represents the first time such a complex is assembled and characterized. NTD is expected to maintain the structural and spectroscopic features of the N-terminal domain of OCP^R[15]. NTD alone also maintains the capacity to trigger quenching in CK, as shown by the strong reduction in fluorescence emission in CK-NTD compared to CK (**Fig. S1.A**). The fluorescence decay kinetics of both CK and CK-NTD (**Fig. 2.A, S1.B**) is characterized by a common >ns component, corresponding to an unquenched pool of APCs. While this unquenched pool represents the total population in CK, it

only accounts for ≈20% of the decay in the case of CK-NTD. Indeed in this complex, ≈80% of the decay takes place in a few hundred ps, demonstrating that the binding of NTD to CK creates a large fraction of quenched APCs. Notably, analogous quenching yield and timescale (80% quenching in a few hundred ps) have been reported *in vivo* and *in vitro* in systems where the full OCP is active and bound to CK[31,32]. Consequently our results indicate that NTD drives a quenching mechanism equivalent to the one driven by OCP[R]. This implies that NTD represents the minimal unit required to activate OCP-dependent NPQ in the core of the PBS in cyanobacteria.

To unravel the origin of the quenching in CK-NTD, ultrafast transient absorption (TA) experiments were conducted on both CK and CK-NTD, and the results were compared. We excited preferentially either APC (630 and 694 nm) or canthaxanthin (520 nm) to pinpoint: i) which species dissipates the excitation energy of APC and ii) what is the effect of the binding of NTD to CK on the energetics of canthaxanthin.

The absorption spectra of the samples, and the excitation wavelengths used, are reported in **Fig. 2.B**. In the main manuscript we focus on the results of CK-NTD excited at 694 nm. Equivalent results were obtained for the 520 and 630 nm excitations and are shown in the SI (**Fig. S8**).

The raw TA data (**Fig. 3.A**) agree with what is observed in fluorescence (**Fig. 2.A, S1.B**), namely that CK-NTD is strongly quenched: i.e. the bleach (≈675 nm) mostly decays in 112 ps in CK-NTD, and in 1.54 ns in CK. By applying a global sequential model (**Fig. 3.B**) to the raw TA data in **Fig. 3.A**, we could satisfactorily fit the CK and CK-NTD datasets with 3 and 4 components, respectively. The evolution-associated difference spectra (EADS) obtained from this analysis are reported in **Fig. 3.C**. The first EADS is sub-ps resolution (100 fs) and contains contributions of coherent artefacts. The second EADS is attributed to energy transfer and equilibration between APC chromophores. This component is faster in CK-NTD than in CK (2 ps versus 21 ps), suggesting that a fast event might occur in this time window in the quenched sample. The 1.54 ns component represents the decay of the unquenched fraction of CK in both samples. In CK-NTD this component is minor, while the majority of the decay (≈76%) occurs in 112 ps. Such quenching yield and timescale, systematically observed with each excitation power used (**Fig. S2**), were consistent with our time-resolved fluorescence results (**Fig. S1.B**). As shown by the normalized second and third EADS of CK (**Fig. 3.C**), the two EADS maintain overall the same spectral features: i.e. the combination of the ground state bleach and stimulated emission (≈675 nm) and the excited state absorption (ESA) of the APC bilins (≈400-650 nm). Their only spectral difference consists in the blue shift of the bleach of the third EADS with respect to the second one, which is due to up-hill energy transfer (excitation at 694 nm excites prevalently the most red species). The same blue shift is also observed in CK-NTD (**Fig. 3.C**). However, the third EADS of CK-NTD displays a distinct spectral change with respect to the second EADS also in the ≈400-650 nm region. Such a spectral change observed in 2 ps in CK-NTD is absent in CK.

The spectrum of the (mixture of) species that rises in 2 ps in CK-NTD can be determined via a model numerically equivalent to the sequential one, in which all the species decay in parallel (**Fig. S3.A**). The resulting spectra are called decay-associated difference spectra (DADS) and are presented in **Fig. S3.B**. The species involved in the spectral changes observed in 2 ps and 21 ps in CK-NTD and CK,

respectively, are represented by the second DADS: the bandshift above ≈650 nm indicates energy equilibration taking place between APC680 and APC660 in both CK and CK-NTD. However, at variance with CK, the second DADS of CK-NTD shows a distinct, additional spectral feature which is mostly positive in the ≈400-530 nm range and negative in the ≈530-650 nm one. Such a feature is absent in CK (**Fig. S3.B**) and, given the spectrum, cannot be assigned to APC.

Binding of NTD to CK increases the conformational freedom of canthaxanthin. To understand whether canthaxanthin is involved in the spectral evolution in the ≈400-650 range observed in 2 ps in CK-NTD (**Fig. 3C**), we analyzed the excited state dynamics of CK-NTD after carotenoid excitation (520 nm, **Fig. 2B**). To aid the interpretation of the spectra and lifetimes of canthaxanthin in CK-NTD, TA experiments were also run on the isolated NTD. To limit bias (due to spectral selection[33–35]) in populating the excited states of canthaxanthin, two different excitation wavelengths were used on NTD (475 and 520 nm, **Fig. 2.B**).

To resolve the excited state spectra of cantaxanthin in NTD unbound (NTD sample) or bound to CK (CK-NTD sample), we fitted our TA data with the compartmental models (target analysis) described in detail in the Supporting Methods (SI) and in **Fig. S4, S8**. The spectra obtained are called species-associated difference spectra (SADS).

By comparing the SADS of canthaxanthin in NTD (**Fig. S4**) and CK-NTD (**Fig. S8**), we obtained information on whether the binding of NTD to CK affects the carotenoid energetics. From the S1 spectra of NTD and CK-NTD (**Fig. 4**) we found that while the vibronic-less structure of the ground state bleach (GSB) is maintained in both NTD and CK-NTD (at variance with OCP^O [14,36]), the GSB of CK-NTD is significantly shifted towards lower energies. By comparing the zero-crossing points of the GSB of NTD and CK-NTD (**Fig. 4**), we found that canthaxanthin undergoes a spectral shift of ≈21 nm towards the red, upon binding of NTD to CK.

A large red shift (40 nm) and a vibronic-less structure is also observed in the absorption spectrum of canthaxanthin when the carotenoid is bound to NTD/OCP^R, with respect to OCP^O. In this case, such changes have been rationalized in terms of both structure and environment contributions via a multiscale atomistic approach[36]. In Ref. [36] it was found that the conformational freedom of the terminal rings of canthaxanthin is higher in NTD than in OCP^O. This allows canthaxanthin to populate more frequently conformers with a larger conjugation which, in turn, cause the redshift of the NTD absorption. Therefore, the fact that the spectrum of canthaxanthin is ≈21 nm more red-shifted in CK-NTD than in NTD, is indicative of canthaxanthin entering a binding pocket in CK where the degree of conformational flexibility of the terminal rings changes with respect to both NTD and OCP.

NPQ takes place in the core of the phycobilisome via excitation energy transfer to a singlet excited state of canthaxanthin. To identify the spectrum of the quencher in CK-NTD, compartmental models were applied to fit all the TA datasets acquired on CK and CK-NTD. The complete set of models and the results obtained at different excitation wavelengths and powers are reported in the

Supporting Information. Below we focus on the model applied to the TA data of CK and CK-NTD excited at 694 nm (**Fig. 5.A-C**).

This model is based on the following assumptions:

i)   for the CK-NTD sample, the total population of excited species is modeled with two schemes, also defined as megacomplexes, describing the excited state dynamics of the quenched or the unquenched CK complexes (**Fig. 5.A-C**). This is a heterogeneous model where the relative amount of initial excitation assigned to the quenched/unquenched CK fractions (75/25) is based on the amplitudes of the fluorescence components observed in CK-NTD via TCSPC ($\approx$80/20, **Fig. S1.B**) and the $\approx$76% quenching yield observed via TA (**Fig. 3.C**). For the CK sample, a single homogeneous scheme that models the unquenched CK dynamics is sufficient to fit the TA data. The scheme adopted for unquenched CK is identical in the two samples;

ii)   the pulse at 694 nm preferentially excites the lowest energy APC pigments (APC680) (**Fig. 5.A, 2.B**). Then, APC680 undergoes "uphill" energy equilibration with APC660 and both species decay to the ground state in $\approx$1.5 ns. This lifetime of unquenched APC bilins matches our results (**Fig. 3.C, S1.B**) and previous ones from time-resolved spectroscopy on CK[32,37].

iii)   the model describing the quenched fraction of CK-NTD is identical to that of the unquenched CK, but contains an additional energy transfer pathway (**Fig. 5.A**). Specifically, APC660 (in equilibrium with APC680) transfers excitation in 111 ps to an unidentified state, here called S_q. S_q is a dissipative channel that decays back to the ground state in 17 ps.

Full details of the schemes and rates used for this analysis are provided in the SI. In **Fig. S6** and, in **Fig. S7**, it is shown that this model provides an excellent fit of our TA data.

This model agrees with the conclusions of several *in vitro* and *in vivo* fluorescence studies[32,38], which identify APC660 as the site of NPQ in cyanobacteria. This conclusion is further supported by the recent OCP-PBS structure[27], which shows NTD interacting more closely with the CK ApcA/ApcB bilins that emit at 660 nm (APC660). Additionally, our models provide experimental evidence that the OCP-related quenching of cyanobacterial PBSs follows an inverted kinetics regime – *i.e.* a slow transfer (111 ps) to a fast decaying quencher (17 ps) (**Fig. 5.A**) – similarly to what was previously found in a variety of photosynthetic light-harvesting complexes of plants[39–42], mosses[43] and algae[44], and proposed based on the recent OCP-PBS structure[27].

What is the quencher in cyanobacteria? The SADS of the quencher S_q, together with those of APC660 and APC680, are presented in **Fig. 5.D**. The SADS of S_q shows a bleach between $\approx$400-530 nm and a positive ESA between $\approx$530-650 nm. This is the region where we observed a spectral change via global analysis (**Fig. 3.C, S3.B**). Importantly, the spectral features characteristic of S_q in the whole $\approx$400-650 nm range are absent in the SADS of both APC660 and APC680.

If S_q cannot be assigned to an APC excited state, can it be assigned to a canthaxanthin one? This possibility is explored in **Fig. 6**. The S1 SADS retrieved for canthaxanthin in CK-NTD (**Fig. S8**) does not correspond to S_q. Indeed the spectrum of S1 is significantly red-shifted compared to S_q ($\approx$83 nm, as measured

from the zero-crossing points). However, S1 is not the only excited state of canthaxanthin. Indeed, another dark state called S* has been systematically identified in canthaxanthin in solvents of different polarity[45,46], in OCP[34], NTD (**Fig. S4**), homologs of NTD[33,34], and in hECN binding OCP[16]. S* differs both in spectrum and lifetime from S1. While its origin remains controversial, several independent studies have assigned its origin to a singlet excited state associated to a distinct conformer of the carotenoid (populated via a distortion of the conjugated chain)[16,34,39,47,48]. In agreement with this proposal, S* has been found functional both as an excitation energy donor and as an acceptor in a variety of natural and artificial antenna systems[39,40,49,50]. Other studies have assigned the origin of the S* spectral feature to a hot ground state, instead[51,52]. The S* spectrum of canthaxanthin shows a bleach in the 400-520 nm region, and displays an excited state absorption starting from ≈520 nm towards longer wavelengths (**Fig. S4**). Strikingly, this corresponds to the region in which the bleach and excited state absorption of S_q lie and, indeed, the spectra of S* and S_q match to a great extent (**Fig. 6**). The S* lifetime of canthaxanthin has been reported to be dependent on the excitation wavelength[33,46] and consistently longer than that of S1, in all environments and at all excitation wavelengths [33,45,46,53]. This is also the case in our NTD experiments, which show that the lifetime of S* is longer than that of S1 (17 ps vs 3.5 ps, respectively) (**Fig. S4**). By assigning the lifetime of S* to S_q, an excellent fit of the TA data of CK-NTD was obtained (**Fig. S6-S8**). Given the striking similarity in spectra and decay rates, we conclude that a singlet excited state of canthaxanthin with the characteristics of S* is responsible of quenching CK, when NTD is bound to it (**Fig. 6**).

Conclusions
In this work we assembled *in vitro* a functional complex in which the carotenoid-binding active domain of OCP, NTD, is bound to the putative quenching site of the phycobilisome – the core. We showed that this minimal system triggers a quenching mechanism with efficiency and rate identical to the ones of the quenching activated by the full OCP on the phycobilisome core *in vitro* and *in vivo*. Our results indicate that when NTD binds to CK, canthaxanthin enters a binding pocket in which the conformational disorder of its terminal rings is enhanced, as supported by the red shift of its absorption (+≈21 nm). The increased conformational freedom, in turn, enables the activation of quenching in CK via a structural switch of the carotenoid: more in detail, we showed that quenching takes place via excitation energy transfer from the singlet excited state of APC phycobylins to a singlet excited state of canthaxanthin. Canthaxanthin accesses this state by changing structure. To date, CK-NTD represents both the largest quenched system (72 bilin pigments per core plus one ketocarotenoid per NTD) and the first one composed of two distinct subunits (CK plus NTD), in which the dissipative mechanism has been identified.

Because an equivalent mechanism of quenching: i.e. excitation energy transfer to a carotenoid singlet excited state, has been recently demonstrated in plants[39–41,54], algae[44] and mosses[43], our results suggest that a common strategy for photoprotection has evolved from their cyanobacterial ancestors.

Methods

Sample isolation. Recombinant holo-NTD was produced in canthaxanthin-producing *E. coli* BL21 (DE3). The expression method used to obtain the holo-proteins was described previously[12]. The CK complex was purified from a Synechocystis PCC 6803 mutant, lacking the PBS rods, as described elsewhere[24]. The CK-NTD complex was prepared by mixing CK at 0.05μM, NTD 1 μM (20 per CK) in phosphate buffer 1.2M (final volume was 5mL) at RT for 10 minutes. The formation of the complex was followed by measuring the decrease of CK fluorescence before and after the addition of NTD using excitation at 600 nm. To separate the complex from the free NTD, CK-NTD was precipitated by ultracentrifugation at 48000 rpm at 23°C for 3 hs. Then, the CK-NTD complex was resuspended in phosphate buffer 1.2M to a final optical density of 4.5 at 630 nm.

Ultrafast spectroscopy experiments and analyses. TA measurements were run on the setup described in Ref.[16] with some modifications. Amplified mode-locked pulses centered at ≈800 nm were generated at 1 kHz repetition rate by a Ti:sapphire Libra system (Coherent) and splitted (80/20) in pump and probe paths, respectively. Depending on the experiment, the pump wavelength was tuned to 475, 520, 630, 694 nm, via optical parametric amplification in an OperA SOLO system (Coherent), and further reduced to 10 nm FWHM using interference filters (THORLABS). The time delay was controlled via an optical delay line up to ≈1 ns, by delaying the pump. The probe white-light continuum was generated by focusing the 800 nm-pulse in a CaF_2 plate, mounted on a home-built rotating stage to avoid damage. The probe was dispersed via a prism spectrograph on a 1024-pixels back-thinned FFT-CCD detector (S7030-1006, Hamamatsu). Pump and probe polarizations were set at magic angle (54.7°). Data were collected on a shot-to-shot basis, and the pump and probe pulses were modulated at frequencies of 500 and 250 Hz, respectively, using mechanical choppers (THORLABS). The optical density of the samples was set to ≈4 cm^{-1} in the case of CK and NTD and ≈2 cm^{-1} in the case of CK-NTD. The sample was kept at room temperature in a 2-mm quartz cuvette and refreshed via a home-built shaker throughout the measurement. Sample integrity was checked by inspecting the signal stability over multiple scans. Experiments with different excitation powers were conducted on both CK and CK-NTD to obtain datasets with an increasing signal-to-noise ratio. In all cases we were able to completely or largely prevent singlet-singlet annihilation effects, depending on the case, as shown in Fig. S5 and explained in the Supporting Methods in the SI. These power-dependent experiments allowed us not only to quantify the amount of singlet-singlet annihilation, but also to produce a compartmental model (target analysis) where power dependency, when present, is accounted for (Supporting Methods in the SI). Multiple scans were acquired at each experiment and averaged before global or target analysis. Global and target analyses were applied to the TA data following the principles reported in Ref.[55] and explained in detail in the Results section. The instrument response function (IRF) of the experiments was estimated from the fitting to be ≈160 fs FWHM. The ultrafast time constants (<<100 fs) and the ones slower than 1 ns were fixed in the global analyses, due to the time resolution of the experiments. In each analysis, the chirp of the supercontinuum probe was corrected for via a parametric description of the IRF.

References

1. Muller, P. Non-Photochemical Quenching. A Response to Excess Light Energy. *Plant Physiol.* **125**, 1558–1566 (2001).
2. Demmig-Adams, B., Garab, G., Adams III, W. & Govindjee, U. *Non-photochemical quenching and energy dissipation in plants, algae and cyanobacteria*. vol. 40 (Springer, 2014).
3. Scanlan, D. J. *et al.* Ecological genomics of marine picocyanobacteria. *Microbiol. Mol. Biol. Rev.* **73**, 249–299 (2009).
4. Niyogi, K. K. & Truong, T. B. Evolution of flexible non-photochemical quenching mechanisms that regulate light harvesting in oxygenic photosynthesis. *Curr. Opin. Plant Biol.* **16**, 307–314 (2013).
5. Zhang, J. *et al.* Structure of phycobilisome from the red alga Griffithsia pacifica. *Nature* **551**, 57–63 (2017).
6. Arteni, A. A., Ajlani, G. & Boekema, E. J. Structural organisation of phycobilisomes from Synechocystis sp. strain PCC6803 and their interaction with the membrane. *Biochim. Biophys. Acta (BBA)-Bioenergetics* **1787**, 272–279 (2009).
7. Adir, N. Elucidation of the molecular structures of components of the phycobilisome: reconstructing a giant. *Photosynth. Res.* **85**, 15–32 (2005).
8. Kirilovsky, D. & Kerfeld, C. A. Cyanobacterial photoprotection by the orange carotenoid protein. *Nat. plants* **2**, 1–7 (2016).
9. Wilson, A. *et al.* A soluble carotenoid protein involved in phycobilisome-related energy dissipation in cyanobacteria. *Plant Cell* **18**, 992–1007 (2006).
10. Kerfeld, C. A. *et al.* The crystal structure of a cyanobacterial water-soluble carotenoid binding protein. *Structure* **11**, 55–65 (2003).
11. Wilson, A. *et al.* Structural determinants underlying photoprotection in the photoactive orange carotenoid protein of cyanobacteria. *J. Biol. Chem.* **285**, 18364–18375 (2010).
12. De Carbon, C. B., Thurotte, A., Wilson, A., Perreau, F. & Kirilovsky, D. Biosynthesis of soluble carotenoid holoproteins in Escherichia coli. *Sci. Rep.* **5**, 1–8 (2015).
13. Kuznetsova, V. *et al.* Comparative ultrafast spectroscopy and structural analysis of OCP1 and OCP2 from Tolypothrix. *Biochim. Biophys. Acta (BBA)-Bioenergetics* **1861**, 148120 (2020).
14. Wilson, A. *et al.* A photoactive carotenoid protein acting as light intensity sensor. *Proc. Natl. Acad. Sci.* **105**, 12075–12080 (2008).
15. Leverenz, R. L. *et al.* A 12 Å carotenoid translocation in a photoswitch associated with cyanobacterial photoprotection. *Science (80-.).* **348**, 1463–1466 (2015).
16. Konold, P. E. *et al.* Photoactivation mechanism, timing of protein secondary structure dynamics and carotenoid translocation in the Orange Carotenoid Protein. *J. Am. Chem. Soc.* **141**, 520–530 (2018).
17. Gupta, S. *et al.* Local and global structural drivers for the photoactivation of the orange carotenoid protein. *Proc. Natl. Acad. Sci.* **112**, E5567–E5574 (2015).
18. Liu, H. *et al.* Dramatic domain rearrangements of the cyanobacterial orange carotenoid protein upon photoactivation. *Biochemistry* **55**, 1003–1009 (2016).

19. Gupta, S. *et al.* X-ray radiolytic labeling reveals the molecular basis of orange carotenoid protein photoprotection and its interactions with fluorescence recovery protein. *J. Biol. Chem.* **294**, 8848–8860 (2019).

20. Bondanza, M., Cupellini, L., Faccioli, P. & Mennucci, B. Molecular mechanisms of activation in the orange carotenoid protein revealed by molecular dynamics. *J. Am. Chem. Soc.* **142**, 21829–21841 (2020).

21. Maksimov, E. G. *et al.* Fluorescent labeling preserving OCP photoactivity reveals its reorganization during the photocycle. *Biophys. J.* **112**, 46–56 (2017).

22. Moldenhauer, M. *et al.* Assembly of photoactive orange carotenoid protein from its domains unravels a carotenoid shuttle mechanism. *Photosynth. Res.* **133**, 327–341 (2017).

23. Chukhutsina, V. *et al.* Light activation of Orange Carotenoid Protein reveals initial C8′-C7′ double bond trans/cis photoisomerization. *bioRxiv* (2022).

24. Gwizdala, M., Wilson, A. & Kirilovsky, D. In vitro reconstitution of the cyanobacterial photoprotective mechanism mediated by the Orange Carotenoid Protein in Synechocystis PCC 6803. *Plant Cell* **23**, 2631–2643 (2011).

25. Harris, D. *et al.* Orange carotenoid protein burrows into the phycobilisome to provide photoprotection. *Proc. Natl. Acad. Sci.* **113**, E1655–E1662 (2016).

26. Jallet, D. *et al.* Specificity of the cyanobacterial orange carotenoid protein: influences of orange carotenoid protein and phycobilisome structures. *Plant Physiol.* **164**, 790–804 (2014).

27. Dominguez-Martin, M. A. *et al.* Structure of the quenched cyanobacterial OCP-phycobilisome complex. *bioRxiv* (2021).

28. Muzzopappa, F. & Kirilovsky, D. Changing color for photoprotection: the orange carotenoid protein. *Trends Plant Sci.* **25**, 92–104 (2020).

29. Elmorjani, K., Thomas, J.-C. & Sebban, P. Phycobilisomes of wild type and pigment mutants of the cyanobacterium Synechocystis PCC 6803. *Arch. Microbiol.* **146**, 186–191 (1986).

30. Ajlani, G., Vernotte, C., DiMagno, L. & Haselkorn, R. Phycobilisome core mutants of Synechocystis PCC 6803. *Biochim. Biophys. Acta (BBA)-Bioenergetics* **1231**, 189–196 (1995).

31. Maksimov, E. G. *et al.* The time course of non-photochemical quenching in phycobilisomes of Synechocystis sp. PCC6803 as revealed by picosecond time-resolved fluorimetry. *Biochim. Biophys. Acta (BBA)-Bioenergetics* **1837**, 1540–1547 (2014).

32. Tian, L. *et al.* Picosecond kinetics of light harvesting and photoprotective quenching in wild-type and mutant phycobilisomes isolated from the cyanobacterium Synechocystis PCC 6803. *Biophys. J.* **102**, 1692–1700 (2012).

33. Khan, T. *et al.* Excited-State Properties of Canthaxanthin in Cyanobacterial Carotenoid-Binding Proteins HCP2 and HCP3. *J. Phys. Chem. B* **124**, 4896–4905 (2020).

34. Khan, T., Kuznetsova, V., Dominguez-Martin, M. A., Kerfeld, C. A. & Polívka, T. UV Excitation of Carotenoid Binding Proteins OCP and HCP: Excited-State Dynamics and Product Formation. *ChemPhotoChem* **6**, e202100194 (2022).

35. Niziński, S. *et al.* Unifying Perspective of the Ultrafast Photodynamics of Orange Carotenoid Proteins from Synechocystis: Peril of High-Power

Excitation, Existence of Different S* States, and Influence of Tagging. *JACS Au* **2**, 1084–1095 (2022).

36. Bondanza, M., Cupellini, L., Lipparini, F. & Mennucci, B. The multiple roles of the protein in the photoactivation of Orange Carotenoid Protein. *Chem* **6**, 187–203 (2020).

37. Van Stokkum, I. H. M. *et al.* A functional compartmental model of the Synechocystis PCC 6803 phycobilisome. *Photosynth. Res.* **135**, 87–102 (2018).

38. Tian, L. *et al.* Site, rate, and mechanism of photoprotective quenching in cyanobacteria. *J. Am. Chem. Soc.* **133**, 18304–18311 (2011).

39. Liguori, N. *et al.* Different carotenoid conformations have distinct functions in light-harvesting regulation in plants. *Nat. Commun.* **8**, (2017).

40. Mascoli, V. *et al.* Capturing the Quenching Mechanism of Light-Harvesting Complexes of Plants by Zooming in on the Ensemble. *Chem* **5**, 2900–2912 (2019).

41. Son, M., Pinnola, A., Gordon, S. C., Bassi, R. & Schlau-Cohen, G. S. Observation of dissipative chlorophyll-to-carotenoid energy transfer in light-harvesting complex II in membrane nanodiscs. *Nat. Commun.* **11**, 1–8 (2020).

42. Ruban, A. V *et al.* Identification of a mechanism of photoprotective energy dissipation in higher plants. *Nature* **450**, 575–578 (2007).

43. Pinnola, A. *et al.* Electron transfer between carotenoid and chlorophyll contributes to quenching in the LHCSR1 protein from Physcomitrella patens. *Biochim. Biophys. Acta (BBA)-Bioenergetics* **1857**, 1870–1878 (2016).

44. de la Cruz Valbuena, G. *et al.* Molecular mechanisms of nonphotochemical quenching in the LHCSR3 protein of Chlamydomonas reinhardtii. *J. Phys. Chem. Lett.* **10**, 2500–2505 (2019).

45. Chábera, P., Fuciman, M., Hříbek, P. & Polívka, T. Effect of carotenoid structure on excited-state dynamics of carbonyl carotenoids. *Phys. Chem. Chem. Phys.* **11**, 8795–8803 (2009).

46. Khan, T., Litvín, R., Šebelík, V. & Polivka, T. Excited State Evolution of Keto-carotenoids after Excess Energy Excitation in the UV Region. *ChemPhysChem* (2020).

47. Niedzwiedzki, D. M., Sullivan, J. O., Polívka, T., Birge, R. R. & Frank, H. A. Femtosecond time-resolved transient absorption spectroscopy of xanthophylls. *J. Phys. Chem. B* **110**, 22872–22885 (2006).

48. Kloz, M., Weißenborn, J., Polívka, T., Frank, H. A. & Kennis, J. T. M. Spectral watermarking in femtosecond stimulated Raman spectroscopy: resolving the nature of the carotenoid S* state. *Phys. Chem. Chem. Phys.* **18**, 14619–14628 (2016).

49. Papagiannakis, E., Kennis, J. T. M., van Stokkum, I. H. M., Cogdell, R. J. & van Grondelle, R. An alternative carotenoid-to-bacteriochlorophyll energy transfer pathway in photosynthetic light harvesting. *Proc. Natl. Acad. Sci.* **99**, 6017–6022 (2002).

50. Kodis, G. *et al.* Light harvesting and photoprotective functions of carotenoids in compact artificial photosynthetic antenna designs. *J. Phys. Chem. B* **108**, 414–425 (2004).

51. Balevičius Jr, V., Abramavicius, D., Polívka, T., Galestian Pour, A. & Hauer, J. A unified picture of S* in carotenoids. *J. Phys. Chem. Lett.* **7**, 3347–3352

(2016).

52. Balevičius Jr, V. *et al.* The full dynamics of energy relaxation in large organic molecules: from photo-excitation to solvent heating. *Chem. Sci.* **10**, 4792–4804 (2019).

53. Šlouf, V. *et al.* Ultrafast spectroscopy tracks carotenoid configurations in the orange and red carotenoid proteins from cyanobacteria. *Photosynth. Res.* **131**, 105–117 (2017).

54. Ruban, A. V *et al.* Identification of a mechanism of photoprotective energy dissipation in higher plants. *Nature* **450**, 575–8 (2007).

55. van Stokkum, I. H. M., Larsen, D. S. & van Grondelle, R. Global and target analysis of time-resolved spectra. *Biochim. Biophys. Acta* **1657**, 82–104 (2004).

56. Chang, L. *et al.* Structural organization of an intact phycobilisome and its association with photosystem II. *Cell Res.* **25**, 726–737 (2015).

57. Tian, L., Farooq, S. & van Amerongen, H. Probing the picosecond kinetics of the photosystem II core complex in vivo. *Phys. Chem. Chem. Phys.* **15**, 3146–3154 (2013).
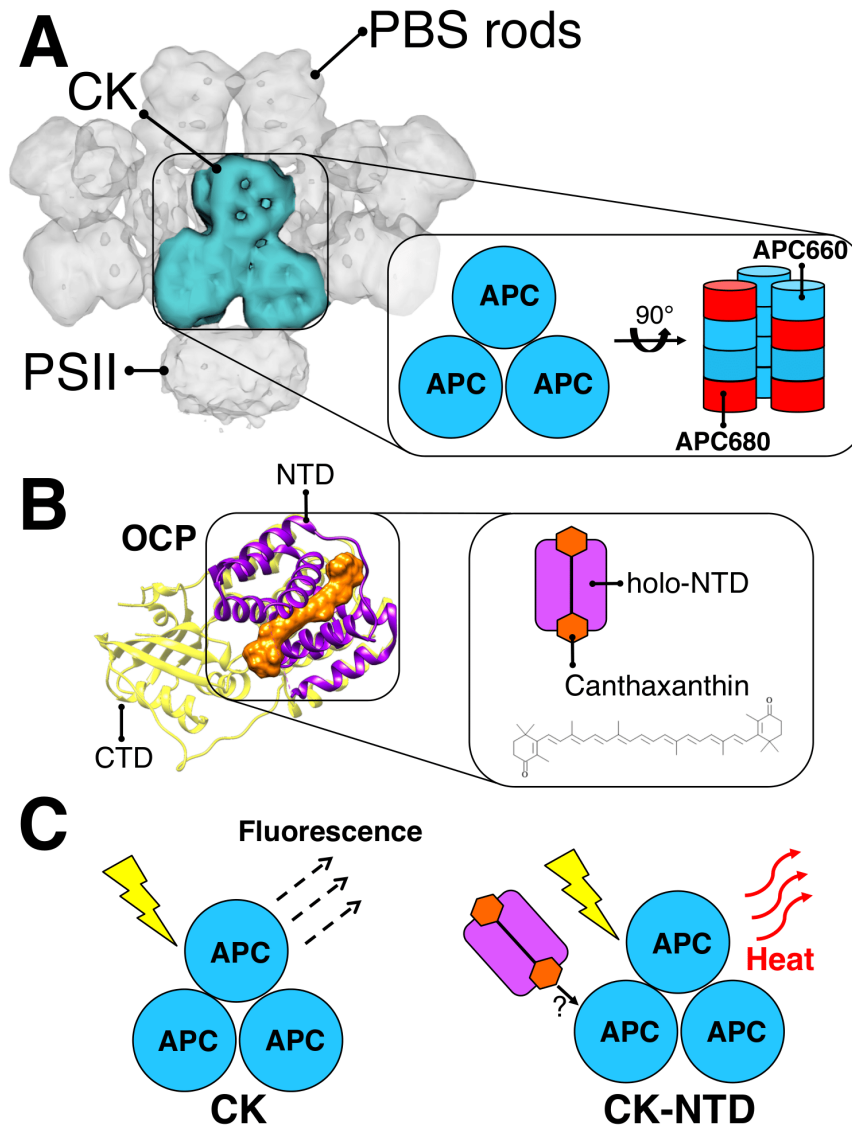
Figure 1. The core of the phycobilisomes and the orange carotenoid protein (OCP). (**A**) In the black quadrant on the right, a model of the isolated cyanobacterial allophycocyanin (APC) core cylinders (CK) is reported. Each cylinder contains 4 disks, for a total of 72 APC pigments. The basal disks contain a total of 6 red APC absorbing at 680 nm (APC680), while the rest absorbs at 660 nm (APC660). On the left, the structure of a complete phycobilisome, including the peripheral rods, in complex with photosystem II (PSII) resolved from *Anabaena* sp. strain PCC 7120[56] is depicted (Electron Microscopy Data Bank, 2822). (**B**) In the black quadrant on the right, a model of the N-terminal domain (NTD) of OCP in its active state is reported. The NTD protein domain, modeled in purple, binds a carotenoid (holo-NTD). The structure of the NTD carotenoid studied in this work, canthaxanthin, is reported in the quadrant. The structure of inactive OCP is shown in yellow (PDB 5UI2)[10] on the left and includes the C-terminal domain (CTD), together with the active domain NTD in purple (PDB 4XB4)[15]. (**C**) On the left, a cartoon of isolated CK set in a light-harvesting state is shown. On the right, the CK-NTD complex, resulting from the association of holo-NTD to CK, is shown (OCP is depicted larger than in real scale for clarity). CK-NTD is strongly quenched. The question mark represents the unknown site of quenching and the unknown effect on the structure and energetics of canthaxanthin, upon binding of NTD to CK.
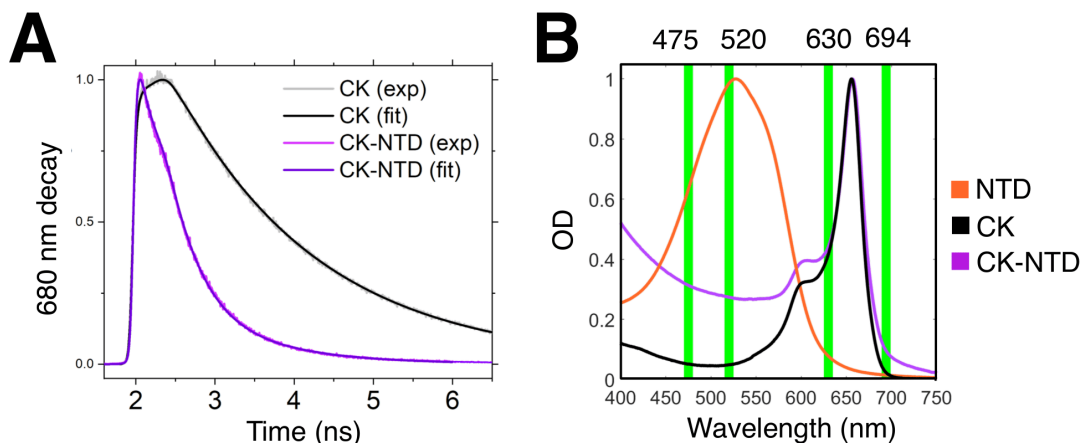
Figure 2. Binding of NTD to CK results in a strongly quenched complex. A. Time-resolved fluorescence of CK and CK-NTD measured with excitation centered at 430 nm and detection at 680 nm. Normalized raw (exp) and fitted kinetics (fit) are displayed. **B.** Normalized absorption spectra of the samples investigated (listed in the legend). The green thick lines indicate the central wavelength (±5 nm) of the excitation pulses used in the TA experiments presented in this work.
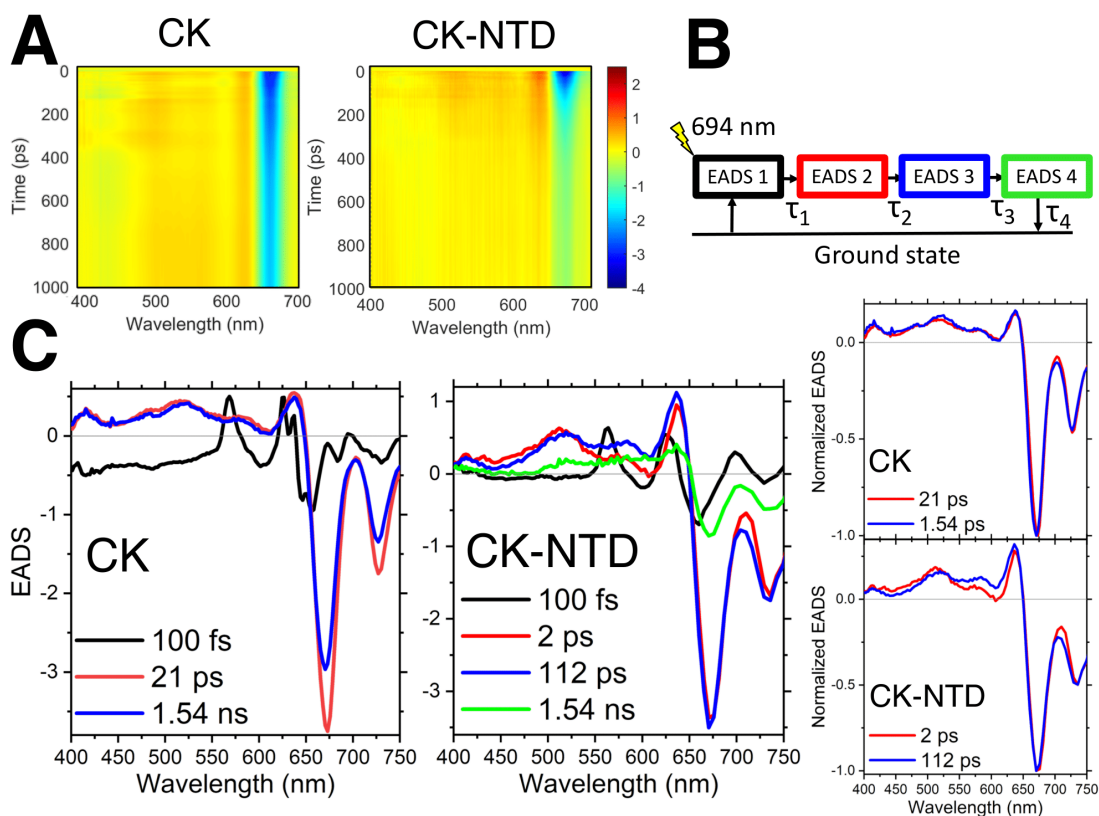

Figure 3. Different excitation energy transfer pathways are present in CK and CK-NTD. A. 2D-raw data maps of the pump-probe experiments on CK and CK-NTD, with excitation at 694 nm at 160 uW. **B.** Global sequential model applied to the 2D-raw data maps in **(A)** to retrieve the Evolution associated Difference Spectra (EADS) reported in **(C)**. **C.** The two full sets of EADS for CK and CK-NTD are shown with the associated lifetimes. The first EADS of CK and CK-NTD have been multiplied by a factor of 0.2 for clarity. The normalized red and blue EADS from the model in **(B)** are reported on the right.
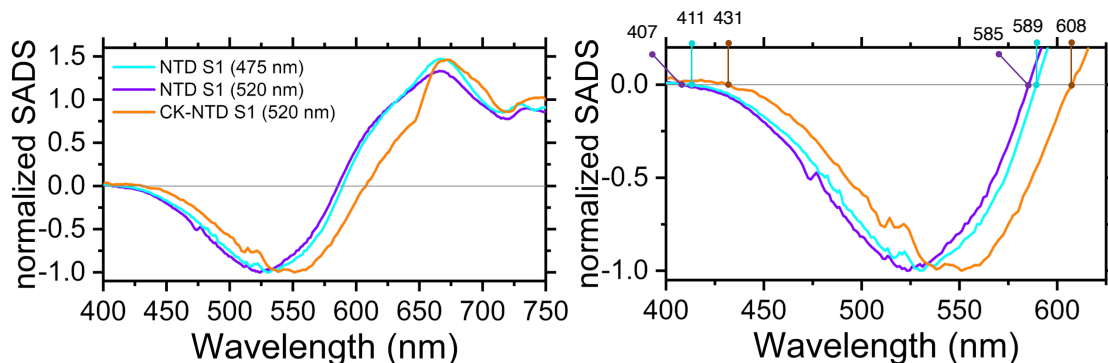
Figure 4. The S1 state of canthaxanthin is red-shifted in CK-NTD with respect to NTD. Left: normalized SADS assigned to the S1 state of canthaxanthin in NTD and CK-NTD, after excitation at 475 nm (NTD) and 520 nm (NTD and CK-NTD), as indicated in the legend. Right: a zoom of the spectra shown on the left, with indicated the zero-crossing points (in nm) used to compute the bandshift of the S1 state of canthaxanthin in CK-NTD with respect to NTD.
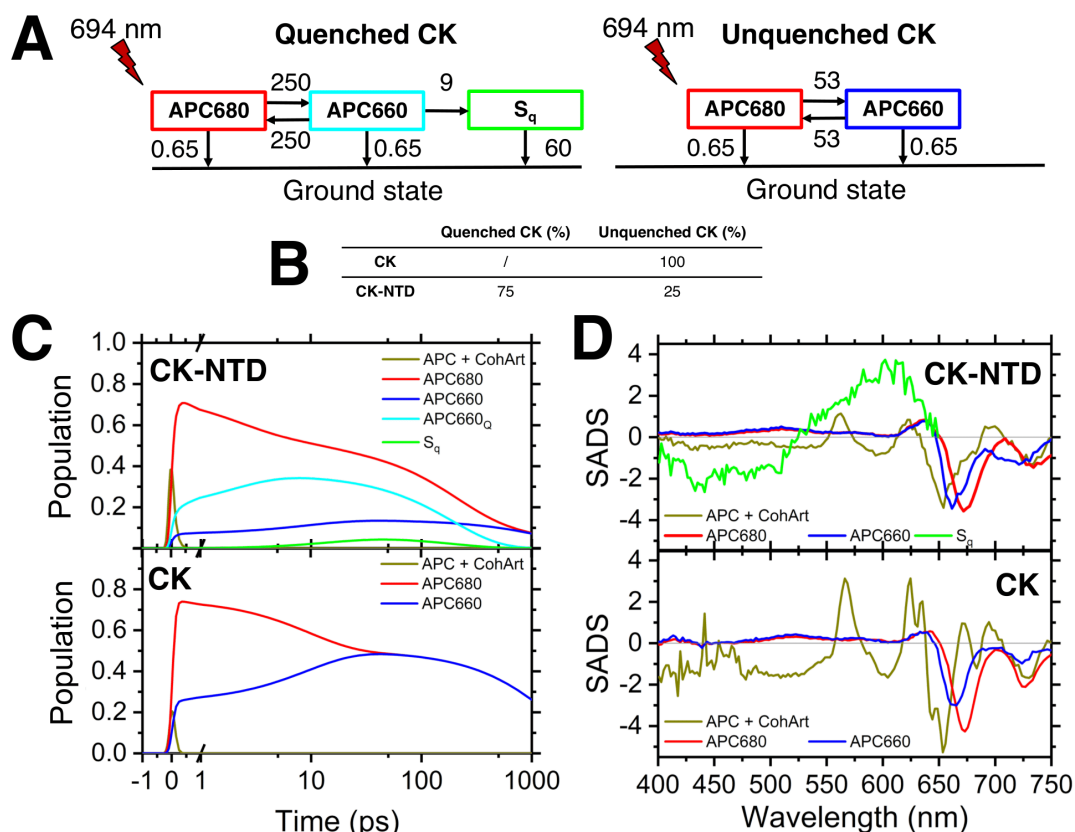

Figure 5. Compartmental model for the 694 nm excitation of CK and CK-NTD.
A. Heterogeneous compartmental model used to fit the TA data of CK and CK-NTD, obtained after excitation at 694 nm in annihilation-free conditions (40 uW). The red bolt indicates the species predominantly excited by the 694 nm excitation (APC680). The heterogeneous model consists of two megacomplexes to describe the excited state dynamics of the quenched and unquenched fractions of CK. Arrows represent energy transfer processes and decays to the ground state. All rates are in ns^{-1}. Kinetics faster than the IRF (<100 fs) were modeled via a precursor species (APC + CohArt) not shown in **(A)** for clarity. The complete model is explained in the Supporting Methods (SI) and in **Fig. S6**. **B.** Distribution

(%) of the quenched and unquenched CK fractions populated by the initial excitation in the CK and CK-NTD samples. **C.** Concentration profiles of all the species included in the compartmental model in **(A)**. The quenched and unquenched APC660 species are labeled as $APC660_Q$ and APC660, respectively. **D.** SADS obtained from the model shown in **(A)**.
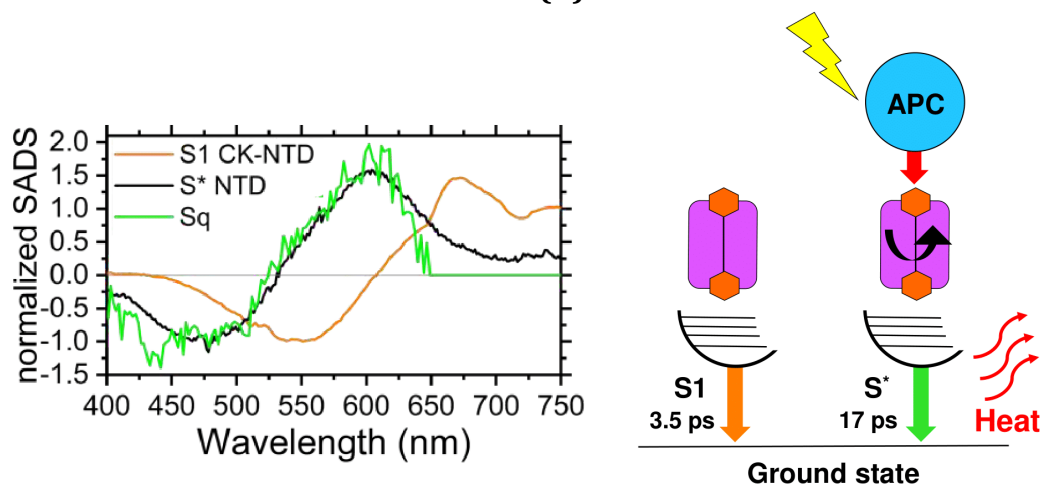

Figure 6. The quencher in CK-NTD is a carotenoid singlet excited state. Left, the SADS of the S_q state (S_q of CK-NTD after excitation at 694 nm, **Fig. 5.D**) is reported together with the SADS of canthaxanthin S1 in CK-NTD (S1 of CK-NTD after excitation at 520 nm, **Fig. S8**) and S^* in NTD (S^* of NTD after excitation at 475 nm, **Fig. S4**). Right: a simplified model of the energetic and conformational landscape of canthaxanthin in CK-NTD is shown. The presence of different singlet excited states (S1 and S* in this case) implies that the carotenoid is set in different conformations in CK-NTD, as indicated by a black curved arrow in the Figure. The quencher of APC (S_q state, **Fig. 5.D**) is here assigned to S^*, due to the striking similarity in spectra and lifetime.

Supporting Information

Supporting methods: compartmental models.
Compartmental models (target analysis) were used to fit the TA datasets obtained upon 694 nm excitation for CK and 630, 520 and 694 nm excitations for CK-NTD. The main features of the compartmental models for the 694 nm excitation are reported in the main text and are here explained more in detail, together with the models applied to the other datasets. To help the reader, we first present the simplest model used in this work: *i.e.* the compartmental model describing the CK sample measured with the most selective excitation (694 nm) and with the lowest excitation power. This model represents the base for the models that include quenching (in the case of CK-NTD) or power-dependent kinetics. All the other models are then introduced step-by-step in the following sections.
The target model used for the TA data of NTD after 475 and 520 nm excitations is shown in **Fig. S4**.

694 nm excitation.
The CK sample. The TA data of the CK sample are fully described by a single scheme (called *Unquenched CK*) containing two compartments of unquenched APC pigments: *i.e.* APC680 and APC660 (**Fig. 5.A, S6.A**). During and immediately after excitation at 694 nm a precursor species is formed, with a lifetime of ≈100 fs. The SADS of this precursor (APC + CohArt SADS, **Fig. 5D, S6.B**) shows multiple positive and negative bands that we tentatively assigned to a combination of excited state absorption (ESA), Raman scattering signal and coherent artifact. From this precursor, 75% and 25% of the excitations are transferred to the APC680 and APC660 compartments, respectively. The equilibration time between APC680 and APC660 (19 ps) is expected to be a weighted average of the intradisk, interdisk and intercylinder equilibration timescales[32,37]. Both APC680 and APC660 decay to the ground state in ≈1.5 ns. This lifetime matches the lifetime of unquenched APC bilins previously measured via time-resolved spectroscopy on CK[32,37] and agrees with our global analyses results (**Fig. 3.C, S1.B**).
The CK-NTD sample. To model the TA data of the CK-NTD sample, an additional megacomplex is required. This megacomplex accounts for the large fraction of quenched CK complexes which, together with a smaller fraction of unquenched CK, is present in the sample. The megacomplexes are called *Quenched CK* and *Unquenched CK*, respectively. The *Unquenched CK* megacomplex is identical for both CK and CK-NTD samples. The relative amount of initial excitation assigned to each scheme (75/25, respectively) has been chosen based on the amplitude of the quenched component measured via TCSPC (80%, **Fig. S1.B**) and TA (76%, **Fig. 3.C**). The *Quenched CK* presents an additional compartment with respect to the *Unquenched CK*. This compartment is assigned to an unidentified species, called S_q. APC660 (which is in equilibrium with APC680) transfers excitation energy to this compartment in 111 ps. S_q decays back to the ground state in 17 ps, quickly dissipating the excitation energy of the *Quenched CK* complexes. The transfer rate from APC660 to S_q has been estimated from the data and agrees with the quenched lifetime component of a few hundred ps measured in previous, independent time-resolved spectroscopy studies on CK[31,57]. Different decay rates have been tested for the quencher S_q, and rates in the range of 60±10 ns^{-1} all resulted in excellent fits with similar RMS error. Given the similarity in spectrum between S_q and the

S* state of NTD (independently estimated, **Fig. S4**), we have then fixed the S_q decay rate to 60 ns^{-1}.

Power dependent study. These simple models fully describes the TA data of CK and CK-NTD obtained at the lowest power (40 μW). To obtain also datasets with a higher signal-to-noise ratio, we additionally measured CK and CK-NTD at higher powers. However, at higher powers, singlet-singlet annihilation might contribute to the excited state dynamics. To understand at which power such contribution should be taken into account in the model, additional independent measurements were run on CK at 694 nm excitation, with a power of 100, 160 and 320 μW. In all cases, the very low absorption cross-section of CK at 694 nm (**Fig. 2.B**), allowed to maintain a significantly low excitation density. Indeed, as in Ref. [40], the excitation density was computed as $\frac{N_{APC} \cdot \Delta OD_{max}}{2 OD_{max}}$, where OD_{max} refers to the Qy region and N_{APC} is the number of APC per single CK. In CK the excitation density ranged between 0.5% (40 μW) and 6.8% (320 μW). Similarly, a power-dependent study with excitation at 694 nm was also conducted on CK-NTD and the excitation densities were estimated to range between 0.96% (40 μW) and 3.2% (160 μW). The time traces of CK and CK-NTD at the different powers are reported in **Fig. S5**. The excitation density is expected to be smaller than these estimates because, for these calculations, the totality of 72 APC pigments was considered to absorb at 694 nm, which is a large overestimation. Only a negligible number of APC pigments is instead expected to absorb significantly at this wavelength (mostly APC680).

These estimates suggest that the contribution of annihilation in all cases was maintained to null or limited values. To properly account for possible annihilation, we applied a modified scheme to the model presented in **Fig. 5.A** to each CK dataset. In the modified model (**Fig. S6.B**) an additional megacomplex, called *Unquenched CK with annihilation*, is added to the *Unquenched CK* one, in which APC680 decays at a faster rate (25 ns^{-1}). The fraction of CK belonging to the *Unquenched CK with annihilation* scheme at each power is reported in **Fig. S6.C**. This power-dependent model (**Fig. S6.A**) results in remarkably similar SADS amongst all the different powers used (**Fig. S6.B**).

In the case of the CK-NTD sample, two megacomplexes describing the *Unquenched CK with annihilation* and *Quenched CK with annihilation* fractions were added to the model in **Fig. 5.A**, each containing a faster decay of APC680 (25 ns^{-1}). From this model we estimated a contribution of annihilation equal to 0% at 40 μW and 14% at 160 μW.

Spectral assumptions. To limit the number of free parameters, a few spectral assumptions were made, similarly to what previously done in Ref.[39,40]: 1) the SADS of APC680 and APC660 were found to be similar below 649 nm (the ESA region) in CK (**Fig. 5.B**). Therefore, in the target analysis of CK-NTD, the SADS of APC680 and APC660 are guided to be similar (but not identical) below 649 nm (the ESA region); 2) the SADS and decay rate of S_q were linked at 40 and 160 μW in CK-NTD. The SADS of S_q was forced to be zero above 649 nm, to avoid an imprecise estimation of its spectrum in the region were the spectral evolution of the APC bands takes place.

This model resulted in an excellent fit, as can be assessed from the overlap of fitted and measured kinetics across the spectrum (**Fig. S7**).

630 and 520 nm excitations.

In line with the model developed for the 694 nm excitation, compartmental models consisting of *Unquenched* and *Quenched CK* megacomplexes were also used for the TA datasets of the CK-NTD sample, after 630 and 520 nm excitations. The only difference is that both *Unquenched* and *Quenched CK* schemes now contain three APC660 compartments (630 and 520 nm excitations), instead of one (694 nm excitation). APC660$_A$, APC660$_B$, APC660$_C$ represents the top cylinder, APC660 disks in the basal cylinders, and the APC660 in the mixed APC660/APC680 disks, respectively. The equilibration rates chosen for these models were based on the ones previously validated on CK for excitations also selective towards APC660, via independent time-resolved spectroscopy experiments[37] and represent intradisk, interdisk and intercylinder equilibration. The models used for the 630 and 520 nm excitations are presented in **Fig. S8** and the datasets were fitted simultaneously: a precursor is instantaneously excited. This precursor decays in 0.19 ps and transfers the excitation energy to the APC660 compartments. The three APC660 compartments (APC660$_A$, APC660$_B$, APC660$_C$, **Fig. S8**) equilibrate amongst themselves and with APC680, and they all decay with the unquenched APC rate of 0.65 ns^{-1}. The SADS of the APC660 and APC680 species obtained via these models have their bleaches centered at ≈660 nm and ≈680 nm, respectively, as it should be expected and in agreement with the results for the 694 nm excitation (**Fig. 5.B**). Again similarly to the model applied to the 694 nm excitation of CK-NTD (**Fig. 5.A**), in the *Quenched CK* pool, excitation energy is transferred from the APC660 compartments to S$_q$ with rates of 5.6 and 8.9 ns^{-1}. Then, as before, S$_q$ quickly decays to the ground state in 17 ps.

With the 520 nm excitation, NTD is directly excited in addition to CK (**Fig. 2.B**). The direct excitation of NTD was modeled by adding a megacomplex, called *Canthaxanthin*, which describes the excited state dynamics of the carotenoid (**Fig. S8**). The *Canthaxanthin* megacomplex is identical to the one used to model the TA data of the NTD sample after 520 excitation, but it misses the compartment assigned to the S1′ species resolved in the case of NTD (**Fig. S4**). No precursor in the canthaxanthin megacomplex was necessary to be included in the 520 nm excitation models of CK-NTD and NTD.

Spectral assumptions. Similar to the case of the 694 nm excitation (see above), the SADS of S$_q$ is assumed to be zero above 649 nm, and the SADS of APC680 and APC660 are here assumed to be equal in the ESA region. The S$_q$ SADS was guided by the SADS estimated with the 694 nm excitation. The SADS of APC660, APC680 and the NTD S$_q$ have been linked between the two experiments at 630 and 520 nm excitations (**Fig. S8**). This model resulted in an excellent fit, as can be assessed in **Fig. S9**.
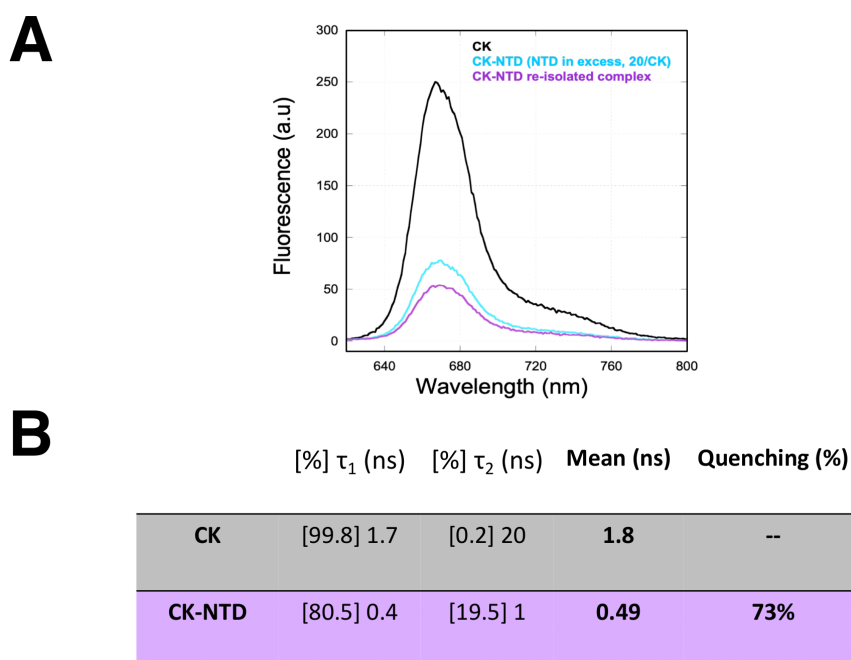
A

B

	[%] τ_1 (ns)	[%] τ_2 (ns)	Mean (ns)	Quenching (%)
CK	[99.8] 1.7	[0.2] 20	**1.8**	--
CK-NTD	[80.5] 0.4	[19.5] 1	**0.49**	**73%**

Figure S1. Quenching of CK upon addition of NTD. A. Steady-state emission spectra of CK (black), CK-NTD (cyan) and after complex re-isolation (purple). CK-NTD complex was prepared by mixing 0.05µM cc CK and NTD 1 µM (20 per CK) in 1.2M phosphate buffer (final volume was 5mL) at RT for 10 minutes. Fluorescence emission spectra of the samples were measured before and after the addition of NTD (the sample was diluted until A655=0.036) using an excitation centered at 600nm. To re-isolate the complex, CK-NTD was precipitated by ultracentrifugation at 48000rpm at 23°C for 3 hs, two times (the excess of NTD remained in the supernatant). **B.** Summary table of the results of the sequential model used to fit the TCSPC measurements on CK and CK-NTD (excitation at 430 nm, emission at 680 nm, kinetics shown in **Fig. 2**). Between brackets, the percent amplitudes of each component are reported, together with the lifetimes in ns.
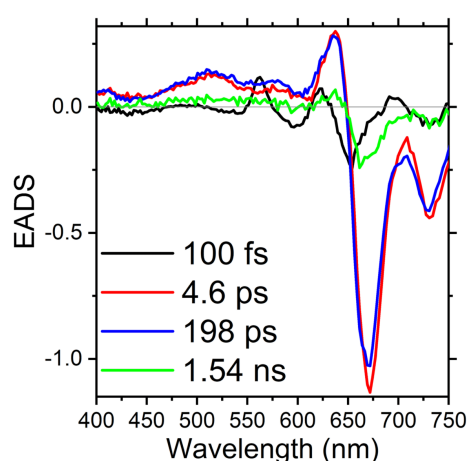

Figure S2. Sequential model applied to CK-NTD excited at 694 nm (40 uW). Evolution Associated Difference Spectra (EADS) obtained fitting the transient absorption (TA) experiments on CK-NTD, upon excitation at 694 nm with the lowest power (40 uW). The first EADS has been multiplied by a factor of 0.2 for clarity.
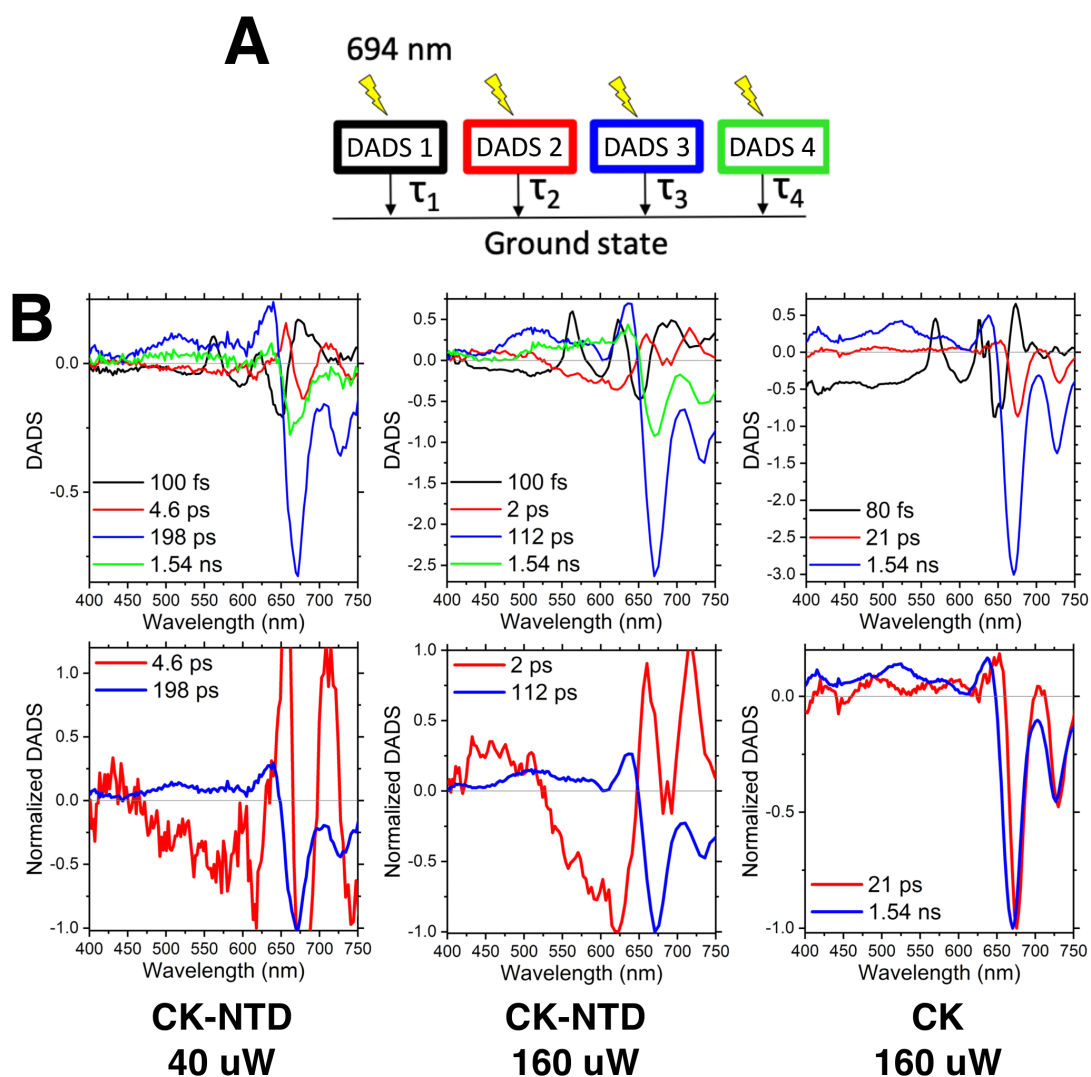
Figure S3. Parallel model for the 694 nm excitation of CK and CK-NTD. A. Scheme of the parallel model applied to obtain the decay associated difference spectra (DADS) shown in **B. B.** The DADS of CK-NTD (at 40 and 160 uW excitation power) and CK (160 uW excitation power) are shown above. Normalized DADS are shown on the bottom for selected components. The samples and excitation power used in each dataset are indicated below the plots. The first DADS have been multiplied by a factor of 0.2 for clarity.
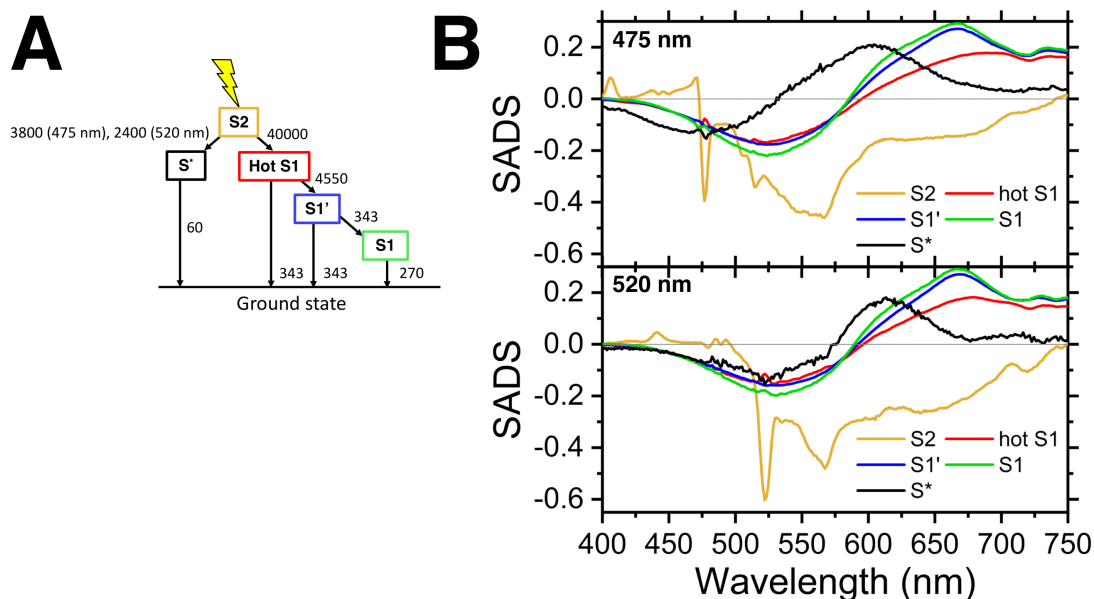
Figure S4. Compartmental model for the 475 and 520 nm excitations of NTD. A. Compartmental model used to fit the TA data of NTD upon excitation at 475 and 520 nm. The yellow bolt indicates that S2 is the first state directly populated following each excitation. The models and rates used to fit the datasets obtained with the 475 and 520 nm excitations are identical, except for the rates of internal conversion from S2 to S* which are estimated independently and are different (as indicated in the scheme). The higher rate at 475 nm excitation agrees with the expected higher probability of S* to be populated in NTD with respect to lower excitation energies (photoselectivity[34,46]). All rates are in ns^{-1}. SADS obtained from the model in **(A)**, at the excitation wavelength indicated on the plot. It must be noted that for this model a compartment called S1', because of the similarity in spectrum and lifetime with S1, was required to obtain an excellent fit of the TA data. After vibrational relaxation from hot S1 to S1', 50% of S1' decays directly to the GS, whereas the remainder relaxes to S1, which in turn decays to the GS in ~4 ps.
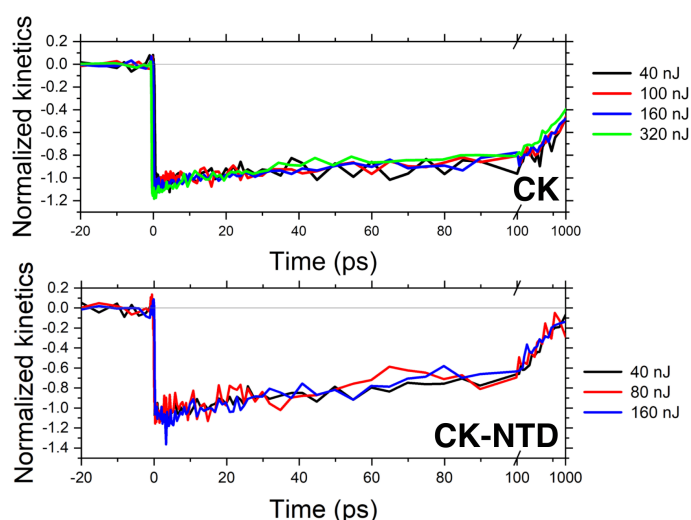

Figure S5. Power-dependent kinetics of CK and CK-NTD. Normalized traces (raw data) at the minimum of the ground state bleach of CK and CK-NTD, obtained independently after excitation at 694 nm, with different energies per pulse (indicated in the legend).
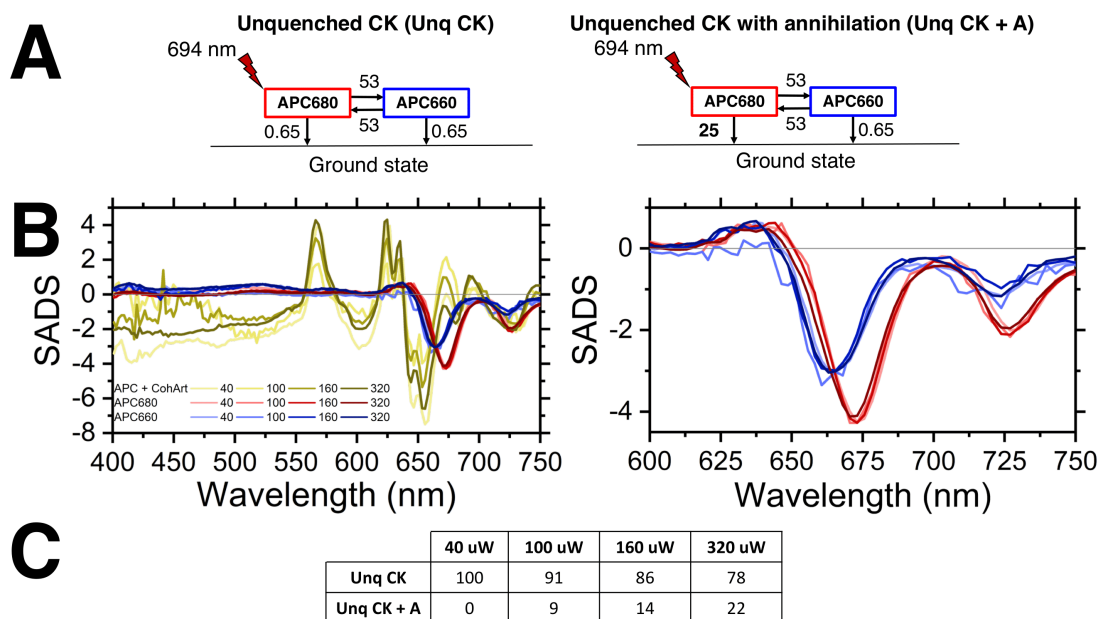
22

Figure S6. Compartmental model for the 694 nm excitation of CK at different powers. A. Compartmental model used to fit the TA data of CK upon excitation at 694 nm at different excitation powers. The precursor (APC+CohArt, see Supporting Methods) is not shown for clarity. All rates are in ns^{-1}. **B.** Complete SADS (left) and a zoom of the bleach region (right), obtained from the model shown in **(A)**. **C.** Relative amount (%) of initial excitation assigned to the *Unquenched CK* (Unq CK) and *Unquenched CK with annihilation* (Unq CK + A) megacomplexes **(A)** at the different excitation powers used, as indicated in the table.
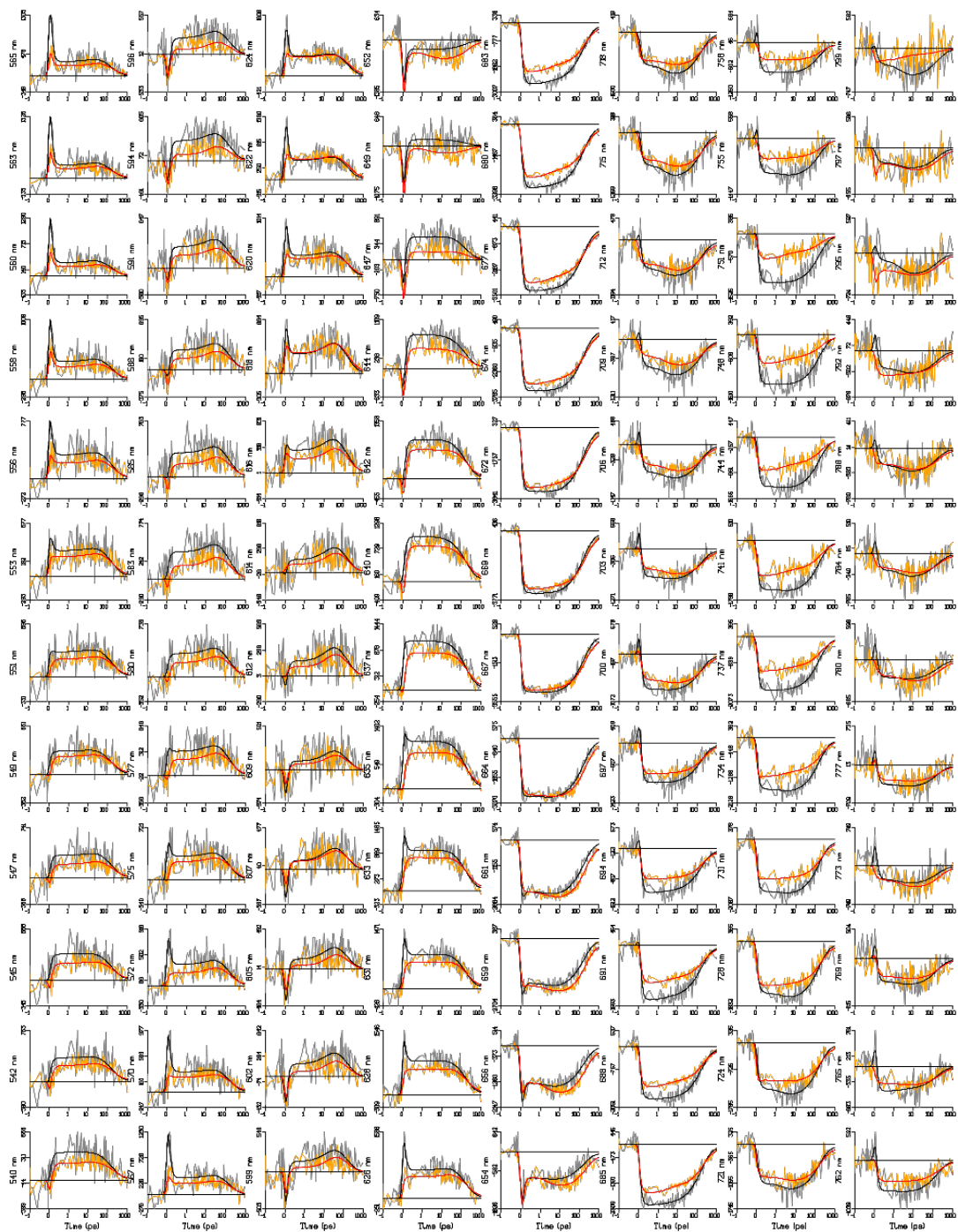
Figure S7. Transient difference absorption of CK-NTD at 96 wavelengths (indicated in the ordinate label) after 694 nm excitation. Color code: 160 uW (grey), 40 uW (orange). Black and red lines indicate the simultaneous target analysis fit. Note that the time axis is linear until 1 ps and logarithmic thereafter. Note also that each panel is scaled to its maximum. Overall root-mean square error of the fit is 107.7 μOD.
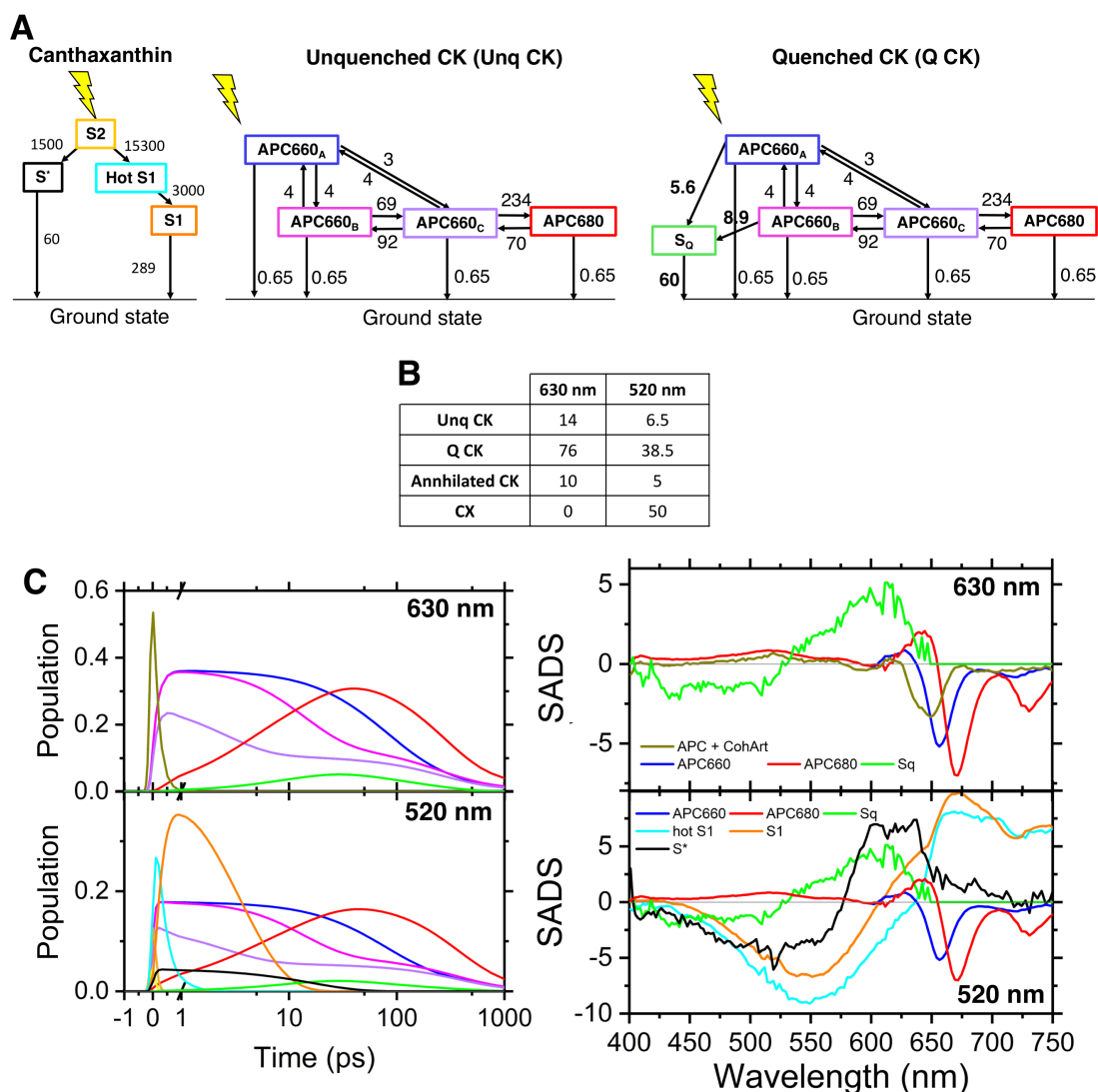
24

Fig. S8. Complete compartmental analysis on the TA data after 630 and 520 nm excitations of CK-NTD. A. Compartmental model used to fit the TA data of CK-NTD upon excitations at 630 and 520 nm. The instantaneous precursor (APC + CohArt) modeled in the 630 nm and 520 nm data (see Supporting Methods) is not shown for clarity. All rates are in ns^{-1}. **B** Relative amount (%) of initial excitation assigned to the *Unquenched CK* (Unq CK), Q*uenched CK* (Q CK) and *Canthaxanthin* (CX) megacomplexes **(A)**, at the different excitation wavelengths used. In both datasets a small fraction of annihilated *Unquenched* and *Quenched CK* was accounted for (10% and 5%, respectively), by setting the APC660$_A$ decays to 14 ns^{-1}. **C.** Concentration profiles (left) and complete SADS (right) obtained from the model shown in **(A)**. The excitation wavelengths to which each plot refers to are indicated on top of the figures. Note that the SADS of APC660, APC680 and the NTD S$_q$ have been linked between the two experiments at 630 and 520 nm excitations and are therefore identical. The SADS of S2 and APC + CohArt (light orange and yellow concentration profiles on the left) are not shown for clarity.
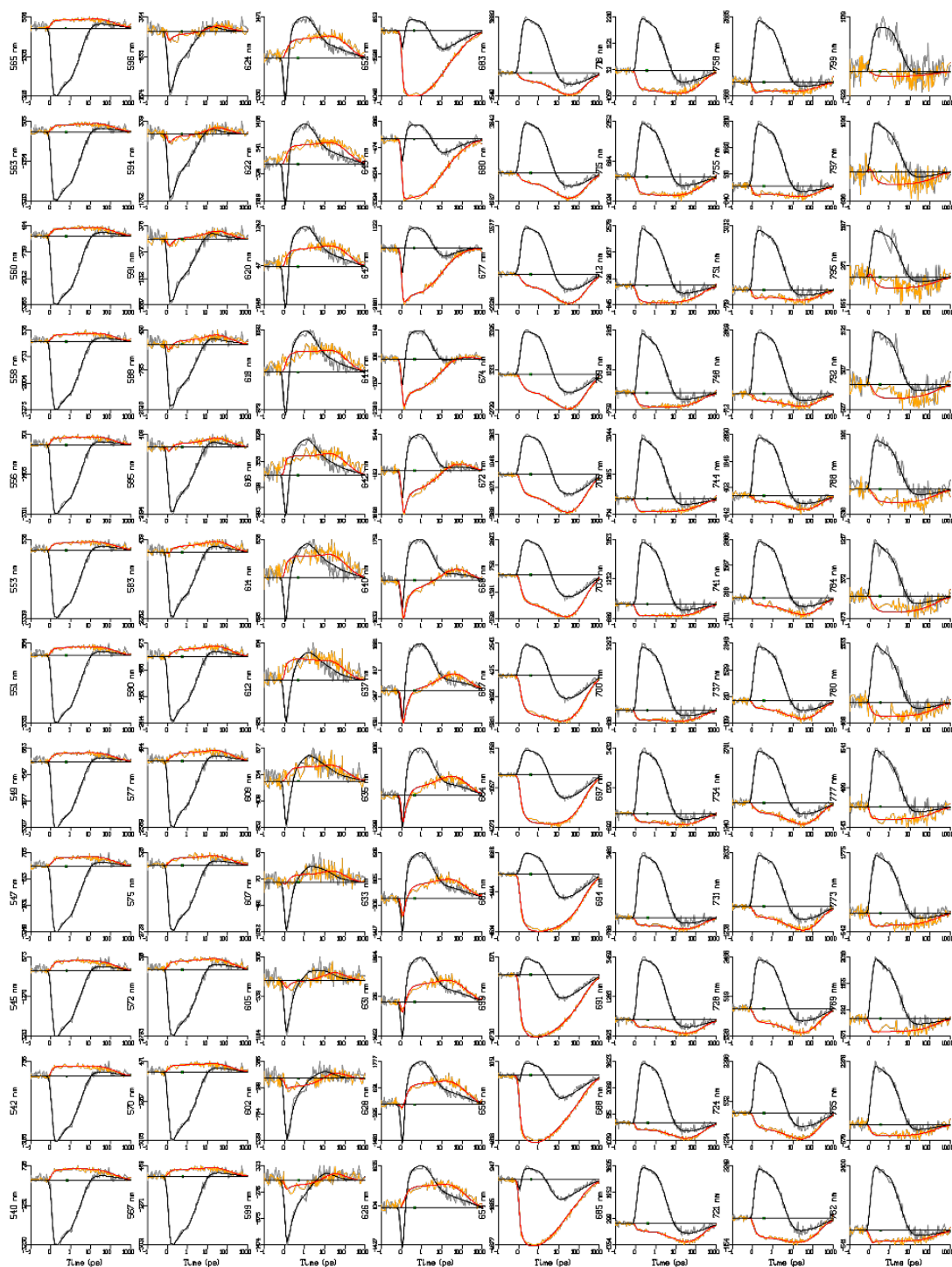
Figure S9. Transient difference absorption of CK-NTD at 96 wavelengths after 520 and 630 nm excitations. Color code: CK-NTD after 520 (grey) and 630 (orange) nm excitations. Black and red lines indicate the simultaneous target analysis fit. Note that the time axis is linear until 1 ps and logarithmic thereafter. Note also that each panel is scaled to its maximum. Overall rms error of the fit was 87.2 µOD.